UCSF
UC San Francisco Previously Published Works

Title

Inhibition, but not excitation, recovers from partial cone loss with greater spatiotemporal integration, synapse density, and frequency

Permalink

https://escholarship.org/uc/item/0fm75301

Journal

Cell Reports, 38(5)

ISSN

2639-1856

Authors

Lee, Joo Yeun
Care, Rachel A
Kastner, David B
et al.

Publication Date

2022-02-01

DOI

10.1016/j.celrep.2022.110317

Peer reviewed

eScholarship.org
Powered by the California Digital Library
University of California

HHS Public Access
Author manuscript
Cell Rep. Author manuscript; available in PMC 2022 February 23.

Published in final edited form as:
Cell Rep. 2022 February 01; 38(5): 110317. doi:10.1016/j.celrep.2022.110317.

Inhibition, but not excitation, recovers from partial cone loss with greater spatiotemporal integration, synapse density, and frequency

Joo Yeun Lee[1,*], **Rachel A. Care**[1], **David B. Kastner**[2], **Luca Della Santina**[1,3,4], **Felice A. Dunn**[1,5,*]

[1]Department of Ophthalmology, University of California, San Francisco, San Francisco, CA 94143-0518, USA

[2]Department of Psychiatry and Behavioral Sciences, University of California, San Francisco, San Francisco, CA 94143-0518, USA

[3]Bakar Computational Health Science Institute, University of California, San Francisco, San Francisco, CA 94143-0518, USA

[4]Present address: College of Optometry, University of Houston, Houston, TX 77204-2020, USA

[5]Lead contact

SUMMARY

Neural circuits function in the face of changing inputs, either caused by normal variation in stimuli or by cell death. To maintain their ability to perform essential computations with partial inputs, neural circuits make modifications. Here, we study the retinal circuit's responses to changes in light stimuli or in photoreceptor inputs by inducing partial cone death in the mature mouse retina. Can the retina withstand or recover from input loss? We find that the excitatory pathways exhibit functional loss commensurate with cone death and with some aspects predicted by partial light stimulation. However, inhibitory pathways recover functionally from lost input by increasing spatiotemporal integration in a way that is not recapitulated by partially stimulating the control retina. Anatomically, inhibitory synapses are upregulated on secondary bipolar cells and output ganglion cells. These findings demonstrate the greater capacity for inhibition, compared with excitation, to modify spatiotemporal processing with fewer cone inputs.

Graphical Abstract

This is an open access article under the CC BY-NC-ND license (http://creativecommons.org/licenses/by-nc-nd/4.0/).

[*]Correspondence: felice.dunn@ucsf.edu (F.A.D.), jooyeun.lee@ucsf.edu (J.Y.L.).

AUTHOR CONTRIBUTIONS

Conceptualization, methodology, software, resources, writing – review & editing, J.Y.L., R.A.C., D.B.K., and F.A.D.; formal analysis, J.Y.L., R.A.C., L.D.S., and F.A.D.; investigation, visualization, J.Y.L., R.A.C., and F.A.D.; data curation; J.Y.L. and R.A.C.; validation, writing – original draft, supervision, project administration, funding acquisition, J.Y.L. and F.A.D.

SUPPLEMENTAL INFORMATION

Supplemental information can be found online at https://doi.org/10.1016/j.celrep.2022.110317.

DECLARATION OF INTERESTS

The authors declare no competing interests.

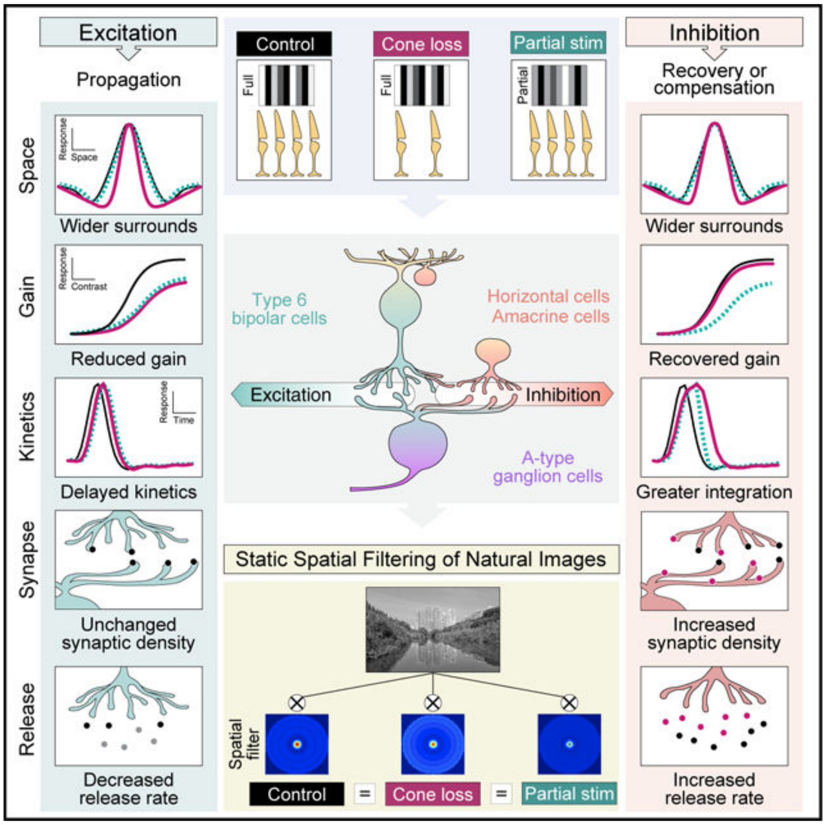
Excitation
Propagation
Control
Full
Cone loss
Full
Partial stim
Partial
Inhibition
Recovery or compensation
Space
Response
Space
Wider surrounds
Wider surrounds
Gain
Response
Contrast
Reduced gain
Recovered gain
Type 6 bipolar cells
Horizontal cells
Amacrine cells
Excitation
Inhibition
Kinetics
Response
Time
Delayed kinetics
A-type ganglion cells
Greater integration
Synapse
Unchanged synaptic density
Static Spatial Filtering of Natural Images
Increased synaptic density
Release
Spatial filter
Decreased release rate
Control
=
Cone loss
=
Partial stim
Increased release rate

In brief

Lee et al. find partial cone loss triggers inhibition, but not excitation, to increase spatiotemporal integration, recover contrast gain, and increase synaptic release onto retinal ganglion cells. Natural images filtered by cone-loss receptive fields perceptually match those of controls. Thus, inhibition compensates for fewer cones to potentially preserve perception.

INTRODUCTION

Neural computations dynamically adapt to a range of stimulus statistics (Kastner and Baccus, 2014; Kim and Rieke, 2001; Weber et al., 2019). Whether and how those adaptive processes could enable robust encoding in response to cell loss is an open question. A circuit ideal for studying this question is the retina for its highly controllable stimuli, well-understood architecture (Helmstaedter et al., 2013; Tsukamoto and Omi, 2017), highly stereotyped responses, and for how it naturally succumbs to cell loss in various disease conditions (Pfeiffer et al., 2020). One of the retina's fundamental computations is the temporal and spatial filtering of its input, photons, through center-surround receptive fields (Barlow et al., 1957; Demb et al., 1999, 2001; Enroth-Cugell and Robson, 1966; Freeman et al., 2015; van Hateren et al., 2002; Olshausen and Field, 2005; Schwartz et al., 2012). How is this retinal computation impacted by cell loss?

To answer this question, we use a system of selective photoreceptor ablation to induce cell death in a fraction of the cones in mature mouse retina without disturbing rods (Care et al., 2019; Shen et al., 2020). Following the loss of 50%–60% of cones, secondary bipolar cells exhibited dendritic remodeling, while their axon terminals remained structurally stable. At the retinal output, the most sensitive of the ganglion cells, the A-type ON-sustained (A_{ON-S}) (Krieger et al., 2017; Margolis and Detwiler, 2007; Smeds et al., 2019; Van Wyk et al., 2009), had spatiotemporal receptive fields, measured from subthreshold voltages, that slowed temporally and widened spatially after partial cone loss (Care et al., 2019). Because the center-surround structure is retained, these findings demonstrate that the computation of spatiotemporal receptive fields is robust up to loss of at least 50% of cones.

Here, we use partial cone ablation to determine the mechanisms that underlie these spatiotemporal modifications. We start by demonstrating the receptive field modifications in both A_{ON-S} and A-type OFF-Sustained (A_{OFF-S}) ganglion cell spikes. Partial ablation of cones could cause both input loss and modifications within the circuit while partial stimulation of the cone array from control retina is used to isolate the effects of input loss alone, as mimicked by light. We show that cone ablation induces functional and structural modifications to inhibitory circuits that could not be recapitulated by partial stimulation. Functionally, inhibitory circuits contribute to wider spatial receptive field surrounds, recovered response gains, longer integration times, and an increased frequency of vesicle release. Structurally, inhibitory synapses onto bipolar cells and ganglion cells increase in density following partial cone loss. While excitatory circuits propagate the input loss, inhibitory circuits increase spatial and temporal integration to recover their responses. Ultimately, the essential computation of center-surround spatial receptive fields is preserved, potentially via these dynamic changes in the inhibitory circuits. Finally, we demonstrate how the recovery of inhibition from input loss in early visual processing has the potential to preserve perception.

RESULTS

Spatial receptive field surrounds of A_{ON-S} and A_{OFF-S} sustained ganglion cells expand after partial cone loss

To determine how spatial processing was affected by input loss, we ablated a subset of cones. We injected diphtheria toxin (DT) into mice expressing the simian DT receptor (DTR) under either S- or M-opsin promoters, which allows for targeted ablation of cones while sparing other cell types in mature retina (Care et al., 2019). We found 63% fewer cones when compared with those found in saline-injected controls (Figures S1A and S1B). To determine the effect of this cone loss on the response properties of identifiable ganglion cells, we made whole-cell patch-clamp recordings from A_{ON-S} and A_{OFF-S} ganglion cells in dorso-nasal retina and stimulated them with bars (Figures 1A and 1F), the intensities of which varied in time with a Gaussian white noise distribution (referred to here as bar noise). The stimulus was designed to preferentially elicit cone-mediated responses with a background to adapt rods (see Method details). In response to the stimulus, spikes (Figures 1B and 1G), subthreshold voltages (Figures 1C and 1H), and excitatory and inhibitory input currents (Figure S2) were used to calculate a linear filter at each bar location to generate a spatiotemporal receptive field for each ganglion cell (Figures 1 and S2) (Care et al., 2019). For each cell, a single spatial receptive field was extracted (see Method details) and fit with a difference of Gaussians to isolate the ganglion cell's center and surround components (Figures 1D, 1E, 1I, and 1J).

The receptive fields of A_{ON-S} ganglion cells in cone-DTR, calculated by spikes, had significantly narrower centers, wider surrounds, and unchanged ratios of center versus surround amplitudes (Figures 1K–1M, closed circles). Similar observations were made in receptive fields calculated from subthreshold voltages (Figures 1K–1M, open circles) (Care et al., 2019). The surround expansion in both spikes and subthreshold voltages was minor but highly significant. The receptive fields of A_{OFF-S} ganglion cells in cone-DTR, calculated by spikes and subthreshold voltages, had significantly wider surrounds and unchanged center widths and ratios of center versus surround amplitudes (Figures 1N–1P). These results indicate that partial cone loss triggers changes in the functional output from A_{ON-S} and A_{OFF-S} ganglion cells. Next, we located the source of such changes with a focus on the A_{ON-S} ganglion cells.

Spatial surround expansion of A_{ON-S} ganglion cells arises from partial cone loss but not from partial light stimulation

To understand if the changes in the spatial receptive fields of A_{ON-S} ganglion cells are from pre-existing mechanisms present in control retina, such as adaptation, or from mechanisms induced by cone loss, we modified the bar noise stimulus described above so that alternating bars were held constant at the background intensity to mimic unresponsive cones (Figure S2) (Care et al., 2019). The other half of the bars flickered to stimulate half of the cones within the ganglion cell's receptive field. Therefore, partial stimulation of cones in control retina will differentiate between mechanisms activated by partial cone stimulation and those activated by partial cone loss. We compared the receptive fields between full and partial stimulation of control retina to determine if the observed changes in cone-DTR retina are induced by input loss and/or by circuit modifications, e.g., by mechanisms that are not activated by partially stimulating photoreceptors in control retina.

To distinguish how losing half of the cones is functionally distinct from stimulating half of the cones, we directly compared the spatial receptive field profiles from excitatory and inhibitory currents between cone-DTR and partial stimulation of control retina and found that partial stimulation of control retina lacks the spatial receptive field modifications observed in cone-DTR retina (Figure S2), demonstrating that the spatial changes observed in cone-DTR retina were not recapitulated by stimulating half of the cones in control retina. The lack of changes in receptive field parameters of both excitatory and inhibitory currents under partial and full stimulation are consistent with previous results in which subthreshold voltage receptive field profiles were constant between partial and full stimulations (Care et al., 2019). Furthermore, when fewer than half the cones were stimulated in control retina, receptive field parameters also failed to recapitulate those measured in cone-DTR retina (data not shown). Therefore, the expansion in the surround widths of both excitatory and inhibitory receptive fields in cone-DTR retina is triggered by mechanisms that originate from inhibitory pathways following partial cone loss.

Gain of voltage and excitatory current decreases while gain of inhibitory current recovers after partial cone loss

To further investigate how responses in the cone-DTR retina are distinct from those in control retina, we made three comparisons of the gain between stimulus input and ganglion cell responses: (1) control versus cone-DTR retina, (2) full versus partial stimulation of control retina, and (3) cone-DTR versus partial stimulation (Figures 2A–2C). We measured the A_{ON-S} ganglion cells' subthreshold voltages and underlying excitatory and inhibitory currents in response to the full and partial bar stimuli. These responses were described by a linear-nonlinear model to encapsulate fundamental retinal computations (Baccus and Meister, 2002), and the linear spatial component was used as above to describe the spatial receptive field. The nonlinear component maps a linearly filtered version of the stimulus to the cell's actual response (see Method details; Figures 2D–2F). The average slope of the nonlinearity reflects the average change in response magnitude to a given change in the stimulus contrast. Thus, we used the slope of the best fit line to each nonlinearity to extract the first-order contrast gain of each A_{ON-S} ganglion cell (Appleby and Manookin, 2019; Kim and Rieke, 2001; Nagy et al., 2021; Ozuysal et al., 2018).

In the first comparison, the gain of the voltages following partial cone loss (cone-DTR) decreased compared with in control retina (Figure 2G, magenta). Similarly, in the second comparison, partial stimulation of control retina resulted in decreased voltage gain when compared with full stimulation of the same control retina (Figure 2G, green). In the third comparison, gain was lower in cone-DTR compared with in partial stimulation of control retina (Figure 2G, black). To directly compare cone-DTR and partial stimulation, we computed the ratio between cone-DTR and control versus the ratio between partial and full stimulation and found that the relative gain in cone-DTR was smaller than in partially stimulated control retina (Figure 2G'), reflecting the results from the third comparison above. Such results could be explained by (1) diminished excitatory synaptic inputs, which would be consistent with cone loss, (2) increased inhibitory synaptic inputs, which would be inconsistent with cone loss, and/or (3) reduced excitability of ganglion cells, which does not have an obvious prediction from cone loss.

To test for changes in excitatory inputs, we compared the gain of the underlying excitatory currents, which originate from the secondary bipolar cells and are the dominant source of the A_{ON-S} ganglion cells' voltage outputs (Figure 2E) (Murphy and Rieke, 2006). In both cone-DTR and partially stimulated control retina, gain was smaller in excitation, indicative of diminished excitatory inputs from cone bipolar cells (Figure 2H). Furthermore, the relative gain of cone-DTR was smaller than the relative gain of partially stimulated control retina, demonstrating an even greater reduction of excitatory inputs in cone-DTR retina (Figure 2H').

Next, we compared the gain of the inhibitory currents, which originate from amacrine cells directly contacting the A_{ON-S} ganglion cell (Figure 2F). In contrast to the reduced voltage and excitatory gain described above, the gain of the inhibitory currents was indistinguishable in cone-DTR and control conditions, whereas the average inhibitory gain was diminished for partially stimulated control compared with for fully stimulated control conditions (Figure 2I). In another representation, we found a greater relative gain in cone-DTR compared to the relative gain in partially stimulated control conditions (Figure 2I’). The greater gain in cone-DTR suggests that inhibitory pathways leading to amacrine-to-ganglion-cell synapses have recovered from cone loss. This recovered gain of inhibition could contribute to the smaller gain of voltage responses.

Finally, another potential source of lower gain of voltage responses is the reduced intrinsic excitability of the ganglion cell. To test for the possibility of altered intrinsic excitability of A_{ON-S} ganglion cells following partial cone loss, we measured their current-to-spike transformation using two independent methods. Under perforated patch configuration, we measured the spikes in response to an injected white noise current (Kim and Rieke, 2001). The current-to-spike transformations, as described by a linear filter and nonlinearity (Figures 3A and 3B), had no significant differences when compared in a permutation test of the control and cone-DTR conditions (Figures 3C and 3D). Results from this direct current injection are consistent with an independent method of calculating the current-to-spike transformations from measurements of spikes (Figures 3E–3G) and excitatory currents (Figures 3H–3J) from the same A_{ON-S} ganglion cells. Stimulating the retina with a cone-preferring family of flashes on a mean background to adapt rods (STAR Methods), we found that while the maximum spike rate (Figure 3G) and excitatory current amplitudes were significantly smaller in ganglion cells from cone-DTR retina (Figure 3J), the spike-to-current ratios were indistinguishable (Figure 3K). These results indicate that the diminished voltage is not due to changes in the intrinsic excitability of A_{ON-S} ganglion cells, but rather it is caused by a reduced cone-mediated input. Taken together, the reduced excitatory input to and maintained intrinsic excitability of A_{ON-S} ganglion cells demonstrate that modifications in inhibition, induced by cone loss, are activated within the retinal circuit prior to ganglion cell integration.

Cone loss slows the kinetics of cone-mediated inhibitory currents in A_{ON-S} ganglion cells

Having implicated inhibition as the dominant source underlying spatial receptive field changes, we next examined whether this recovered inhibition influences the kinetics of ganglion cell responses. While excitatory inputs dominate the voltage output of the A_{ON-S} ganglion cell light response, inhibitory inputs have been shown to influence their kinetics (Eggers and Lukasiewicz, 2011; Murphy and Rieke, 2006; Park et al., 2018). To understand how the inhibitory currents contribute to response kinetics after partial cone loss, we measured the A_{ON-S} ganglion cells’ temporal filters in response to the bar noise stimulus in four conditions (Figures 4A–4C).

Similar to our previous observation in which we found ganglion cells had slower temporal filters in cone-DTR retina (Care et al., 2019), both cone-DTR and partially stimulated control show longer time-to-peak of filters from spikes, subthreshold voltages, and excitatory and inhibitory currents compared with those of their respective control conditions (Figures S4 and S5), resulting in no differences between cone-DTR and partial stimulation of control retina (Figures S4D–S4F). These data indicate that this slowing of the temporal filters in the cone-DTR condition can be recapitulated by partial stimulation of control retina. Secondly, the ON cone bipolar-cell-mediated b-wave of the photopic electroretinogram (ERG) exhibited delayed kinetics in cone-DTR retina (Figures S4G and

S4H), suggesting that delayed kinetics by the bipolar cell output gives rise to the delays in both the excitatory and inhibitory inputs to the ganglion cell.

Next, we examined whether the response duration of A_{ON-S} ganglion cells is affected by the loss of cone inputs. The duration was determined by the integration time of the temporal filters (see Method details) (Figures 4D–4F). The integration time of filters from spikes and subthreshold voltages in cone-DTR retina was comparable to that of control retina, indicating that the integration time was unchanged at the level of retinal output (Figure 4G, magenta, and S5D). Likewise, partial, compared to full, stimulation of control retina showed no differences in the integration time of the ganglion cells' subthreshold voltage temporal filters (Figure 4G, green), consistent with the lack of relative changes between cone-DTR and partial stimulation of control retina (Figure 4G').

Integration times for excitatory current temporal filters were indistinguishable in cone-DTR and partially stimulated control retina compared with in their respective control retina and between cone-DTR and partial stimulation of control retina, which is consistent with the unchanged integration time of voltage responses (Figures 4H and 4H').

While the integration time of inhibitory currents remained unchanged in partial stimulation compared to full stimulation of control retina (Figure 4I, green), we found a greater integration time of inhibitory current temporal filters in cone-DTR compared with those in control retina (Figure 4I, magenta). Furthermore, relative changes in integration times of cone-DTR were greater than of partially stimulated control retina (Figure 4I'). These results suggest that the greater integration time of inhibitory inputs is induced by cone loss but not by half cone stimulation. Taken together, these results suggest that the slower time-to-peak after partial cone loss arises from pre-existing mechanisms induced by partial cone stimulation, while the greater temporal integration of the inhibitory currents arises from modifications induced by partial cone loss. These results are consistent with the recovered gain of inhibitory inputs, which also arises following partial cone loss but not with partial cone stimulation.

Increased inhibitory synapses on bipolar cell axons following cone loss

Thus far, we have demonstrated that acute cone loss elicits functional changes in inhibitory circuits, which give rise to the expansion of surrounds in the cone-mediated receptive field of A_{ON-S} ganglion cells. Next, we aimed to understand whether there were corresponding anatomical changes in inhibitory synapses following partial cone loss. To do this, we examined the anatomical basis of one of the potential sites for change within inhibitory circuits: amacrine-to-bipolar cell synapses, which could account for the surround expansion in excitatory receptive fields via presynaptic inhibition (Figure S2H).

As a measure of synaptic modifications at the level of bipolar cells, we identified ON and OFF cone bipolar cell types labeled in the *Grm6-TdTomato* line and with synaptotagmin II (Syt2) immunostaining, respectively (Figures 5A–5C, S6A, S6F, and S6G). To determine if partial cone loss impacted bipolar cell morphology, we first measured the volume of types 6–8 bipolar cell axon terminals and found no change in ON cone bipolar cells (Figures 5D, S6B, and S6C). To examine the density of postsynaptic inhibitory receptors within cone bipolar cell axon terminals, we quantified gephyrin, a protein which scaffolds both GABAergic and glycinergic receptors, within the axonal terminals of isolated types 6–8 ON bipolar cells and across the population of type 2 OFF bipolar cells (Figures 5B and S6A). While gephyrin density remained constant in type 2 OFF and types 7 and 8 ON bipolar cells (Figures S6D, S6E, and S6H), the density of gephyrin in type 6 bipolar cells increased significantly in cone-DTR retina (Figure 5E), demonstrating a specific increase in inhibitory synapses between amacrine cells and type 6 cone bipolar cells, the major presynaptic partner of A_{ON-S} ganglion cells (Okawa et al., 2014; Schwartz et al., 2012; Tien et al., 2017).

To further examine the structural changes in inhibitory synapses between amacrine cells and bipolar cells following partial cone loss, we immunostained for a presynaptic inhibitory marker, vesicular inhibitory amino acid transporter (VIAAT), and measured the density of VIAAT apposing type 6 bipolar cells (Figure 5C). Similar to the increased inhibitory postsynaptic density, we found a significant increase in VIAAT density in cone-DTR retina (Figure 5F), suggesting enhanced inhibition from amacrine cells onto bipolar cells following partial cone loss. In addition, immunostaining for the excitatory ribbon synapse-associated protein C-terminal binding protein-2 (CtBP2) revealed no significant difference in the number of presynaptic release sites between control and cone-DTR retinas (Care et al., 2019), indicating that bipolar cell output structures were not affected by partial cone loss. These results demonstrate that after cone loss, inhibitory synapses have increased at amacrine-to-bipolar cell synapses, which provides an anatomical basis for (1) reduced excitatory gain and (2) greater surrounds in excitatory inputs to A_{ON-S} ganglion cells.

Inhibitory synapses on A_{ON-S} ganglion cell dendrites increase following cone loss

In search of an anatomical basis of a second potential recovery site within inhibitory circuits, we investigated changes in amacrine-to-ganglion-cell synapses, which could account for the inhibitory surround expansion in receptive fields (Figure S2Q) and/or the recovered gain (Figure 2I). As a measure of inhibitory synaptic changes, we quantified gephyrin within the dendrites of dye-filled A_{ON-S} ganglion cells (Figures 5G and 5H) and found a significantly increased average linear gephyrin density when summed across the dendritic tree (Figure 5I). When gephyrin puncta density was analyzed by the ganglion cell's dendritic eccentricity, density increased over a 12 μm stretch of the distal dendrites in cone-DTR retina (Figure 5J). To confirm the location of increased gephyrin density within the inner plexiform layer (IPL), gephyrin density was quantified as a function of IPL depth, as conventionally defined with the dendritic stratification of A_{ON-S} ganglion cells limited to 62.5% to 92.5% of the entire IPL depth (Figure 5K) (Helmstaedter et al., 2013). Whereas gephyrin density peaks at 83.5% of the IPL in control retina, in cone-DTR retina, gephyrin density peaks at 77.5% of the IPL (Figure 5K), which shows that inhibitory postsynaptic puncta shift closer to the outer ON sublamina, consistent with the greater gephyrin density found in the ganglion cell's distal dendrites (Figure 5J). However, gephyrin density across the entire IPL, irrespective of the A_{ON-S} ganglion cell dendrites, remained constant (Figures S6I and S6J), illustrating that partial cone loss induced local rearrangements of inhibitory synapses rather than global changes in synaptic density.

Given the specific synaptic changes in the position of inhibitory postsynaptic puncta in A_{ON-S} ganglion cells in cone-DTR retina, we further examined the density of inhibitory presynaptic puncta by measuring the linear density of VIAAT apposed to the ganglion cell's dendrites (Figures 5L and 5M). Similar to the changes in inhibitory receptor density, the average density of VIAAT apposed to the dendrites of A_{ON-S} ganglion cells was significantly higher in cone-DTR (Figure 5N). As a function of distance from the soma, the distal dendrites of A_{ON-S} ganglion cells in cone-DTR retina displayed a short (10 μm) but significant increase in presynaptic VIAAT density (Figure 5O). As a function of the conventionally defined IPL depth, the peak VIAAT density was significantly displaced distally in the IPL in cone-DTR compared with in control retina (Figure 5P), while the overall VIAAT density remained unchanged across the entire IPL (Figures S6K and S6L). The observations that (1) presynaptic VIAAT density increased for a short span along the A_{ON-S} ganglion cell dendrites and (2) the location of this peak density shifted distally within the ON sublamina are congruent with the observed changes in inhibitory postsynaptic receptors. Therefore, these results suggest that both the pre- and postsynaptic inhibitory machinery between amacrine cells and A_{ON-S} ganglion cells have been recruited to synaptic sites after partial cone loss. These results demonstrate that inhibitory synapses rearrange at amacrine-to-ganglion-cell contacts, which demonstrates an anatomical basis for changes in inhibitory inputs to ganglion cells.

Frequency of spontaneous vesicle release from bipolar cells decreases while release from amacrine cells increases after partial cone loss

Having found that inhibitory synapses increased at amacrine-to-ganglion-cell contacts, we next investigated whether these anatomical changes had functional correlates. Synaptic release was measured in voltage-clamp recordings of A_{ON-S} ganglion cells either to isolate excitatory currents from bipolar cells (Figure 6A) or inhibitory currents from amacrine cells (Figure 6E). From recording stretches of spontaneous activity, we extracted individual miniature excitatory and inhibitory postsynaptic currents (mEPSCs and mIPSCs, respectively) and determined event amplitudes, frequencies, and integration times (see Method details). Amplitudes of both mEPSCs and mIPSCs are unchanged in cone-DTR retina (Figures 6B and 6F), suggesting that vesicular content and postsynaptic receptors remain intact. In contrast, while the frequency of mEPSCs decreased in cone-DTR (Figure 6C), the frequency of mIPSCs increased (Figure 6G). Since the density of excitatory postsynaptic puncta in A_{ON-S} ganglion cell dendrites remained unchanged in cone-DTR retina (Care et al., 2019), a smaller mEPSC frequency likely reflects a decrease in cone input to the ON cone bipolar cells and/or an increase in presynaptic inhibition, as was observed structurally (Figures 5E and 5F), and therefore a lower presynaptic release rate. On the other hand, the increase in mIPSC frequency reflects the greater density of inhibitory synapses between amacrine and A_{ON-S} ganglion cells in cone-DTR retina (Figures 5G–5P).

To determine if the kinetics of individual synaptic events were affected by cone loss, we measured the integration time of the spontaneous minis. While the integration time of mEPSCs did not change in cone-DTR (Figure 6D), the integration time of mIPSCs increased significantly (Figure 6H). These results are consistent with the unchanged integration time of pooled excitation and the greater integration time of pooled inhibition (Figure

4). We found that while individual synaptic events between bipolar cells and ganglion cells diminish in amplitude, thus reflecting the loss in total cone input, individual synaptic events between amacrine cells and ganglion cells retain their amplitude and increase their frequencies and integration times, thus suggesting a recovery from the loss in cone input.

Potential impact of spatial receptive field changes on perception

The observed surround expansion and greater temporal integration in inhibitory circuits could not be recapitulated by partial stimulation of the cone mosaic in the control retina, providing evidence that these mechanisms were evoked by partial cone loss. Does the compensation in inhibition potentially serve vision? We tested this by using the measured spatial receptive fields of subthreshold voltages obtained under (1) full and (2) partial stimulation of control retina and (3) full stimulation of the retina with half cone loss to transform an image (Figure 7A). Each of the different categories of receptive fields were convolved with natural images of varying sizes (Figures 7B and 7C) (Tkačik et al., 2011), and we compared the similarities between the resulting images with the original image using two metrics: (1) a rudimentary comparison of mean squared error and (2) a perceptually relevant structural similarity index (Wang et al., 2004). With both metrics, as the spatial receptive fields measured under full and partial stimulation of control retina are statistically equivalent, the images filtered by full and partial stimulation conditions were also similar across a range of image sizes. With the mean squared error index, images convolved with the cone-DTR filter exhibit differences across the majority of image sizes (Figure 7D); however, with the structural similarity index, images convolved with the cone-DTR filter were indistinguishable from those of control conditions across image sizes (Figure 7E). Remarkably, these results suggest that although images transformed by the cone-DTR filter are rudimentarily different from images transformed by the control filters, perceptually, these transformed images may be indistinguishable between control and cone-loss conditions.

DISCUSSION

Recovery by spatial and temporal integration

While changes in inhibitory circuits modified ganglion cell responses in space, gain, and kinetics, the essential computation of center-surround spatial receptive fields of the retinal output remained relatively stable despite losing 50%–60% of the cones (Demb et al., 1999, 2001; Freeman et al., 2015; Schwartz et al., 2012). Are the subtle modifications to ganglion cell response properties a result of the retinal circuit propagating, exacer-bating, or compensating for cone loss? If propagated, ganglion cell responses would directly reflect the degree of cone loss. If exacerbated, ganglion cell responses would be poorer than predicted based on the degree of cone loss. If compensated, ganglion cell responses would be better than predicted based on the degree of cone loss.

Our results demonstrate that inhibitory circuits have compensated for cone loss. Fidelity of weak signals, such as those caused by cone loss, can be increased by greater integration over space and/or time, as has been demonstrated under low mean light (Atick and Redlich, 1990; Enroth-Cugell and Robson, 1966) and even within populations of cells that are tuned to encode weaker signals (Hsu et al., 2021; Kastner and Baccus, 2011; Kastner et al., 2015). Here, we find that at the level of the ganglion cells, both spatial and temporal mechanisms contribute to restoring the overall gain of inhibitory inputs. We assess how these changes in inhibition might impact perception. By using a perceptually based metric to evaluate image similarity between natural images and those convolved with spatial filters directly measured in this study, we infer that the way in which the spatial receptive field has changed preserves perceptually relevant information within an image (Wang et al., 2004). Such results support the possibility that recovery of inhibition in cone-DTR retina compensates for input loss, motivating further elucidation of the effects of greater temporal processing observed in cone-DTR retina on spatiotemporal filtering of natural movies.

Circuit adaptation to stimulation versus cell death

Partial cone loss evokes mechanisms that increase spatial and temporal integration, similar to mechanisms evoked by adaptation; however, the underlying circuits responsible for these mechanisms are likely distinct. At low light levels, adaptation of the retinal circuit causes increased spatial integration by widening the center component (Atick and Redlich, 1990). Such modifications have been attributed to switching from cone-dominated pathways with strong surround circuits to rod-dominated pathways that transmit signals with high degrees of convergence between the rods, interneurons, and ganglion cells, thus creating a broad center, and with minimal surround (Enroth-Cugell and Robson, 1966). Within cone-mediated responses, receptive field centers become monotonically wider, and surrounds become narrower as light levels decrease (Borghuis et al., 2018). In contrast, following partial cone loss, spatial integration increased by only widening the surround at cone-mediated light levels. Here, we attribute these modifications to increased inhibition at the level of feedback to cones via horizontal cells, to bipolar cells via amacrine cells, and to direct amacrine cell inhibition to ganglion cells.

For temporal integration, at low light levels, retinal adaptation causes greater temporal integration by increasing the time-to-peak and integration times of responses (Borghuis et al., 2018; Kim and Rieke, 2001; Van Hateren, 1993; Warrant, 1999). Similar to adaptation at lower light levels, following partial cone loss, inhibitory circuits exhibit increased time-to-peak and integration times, contributing to greater temporal integration. The slower time-to-peak could be attributed to mechanisms that occur with adaptation because the phenomenon (1) arises prior to the level of the ganglion cell and (2) can be recapitulated by partial cone stimulation, in which the retina is in a less light-adapted state (Lee et al., 2021). In contrast, the mechanism that evokes a longer integration time is likely distinct from those evoked by adaptation because the phenomenon is not recapitulated by partial cone stimulation and thus unlikely to arise from a pre-existing mechanism in the control retina.

In this condition of acute photoreceptor loss in mature retina, the remaining circuit increases spatial and temporal integration. The origins of these modifications arise from inhibitory circuits, which contribute to improving the fidelity of signals when inputs have been diminished. The reactions to cone loss, while similar to the effects of adaptation at low light levels, are likely generated by mechanisms distinct from those evoked by adaptation.

Inhibition poised to tune excitatory circuits following perturbation

While excitatory and inhibitory circuits are inextricably linked to work in concert in a fully functioning circuit, following perturbation, these circuits can react independently and reveal their potentially distinct contributions to normal function. As observed in the visual cortex and demonstrated in retina here, the remodeling capacity of inhibitory circuits can exceed that of excitatory circuits in reaction to perturbation (Chen et al., 2012; Saiepour et al., 2015; van Versendaal et al., 2012; Villa et al., 2016). Until inhibitory synapses could be observed simultaneously with excitatory synapses, the relative rates of turnover were unknown. The breakthrough study that accomplished simultaneous live imaging of excitatory and inhibitory synapses showed that, following monocular deprivation, inhibitory puncta onto pyramidal neurons overturned at a faster rate than did excitatory puncta (Villa et al., 2016). This same group found that the plasticity of the visual cortex was directly linked to the structural plasticity of cortical inhibitory neurons (Eavri et al., 2018). Likewise, our findings demonstrate that inhibitory circuits react to partial cone loss more dynamically than excitatory circuits. The center-to-surround amplitude ratios and temporal and gain modifications observed in the excitatory inputs to the ganglion cell following partial cone loss could be mimicked by partial cone stimulation in control retina. In other words, the excitatory circuit equally propagated half the input generated by stimulating half the cones in the control retina or half the signal generated by the remaining cones following partial cone ablation. Functionally, the frequency of mEPSCs in A_{ON-S} ganglion cells decreased, which could arise from changes in pre- and/or postsynaptic functions, e.g., decreases in the total number of synapses, sizes of readily releasable pool of synaptic vesicles, release probabilities, or intracellular calcium concentrations. We speculate that fewer cone inputs affect the rate of spontaneous release or calcium concentration at the cone bipolar cell terminal since the numbers of presynaptic release sites within type 6 bipolar cells and excitatory postsynaptic receptor sites within A_{ON-S} ganglion cells were unchanged in cone-DTR retina (Care et al., 2019).

It seems reasonable to predict that inhibitory circuits should exhibit similar functional changes observed in the excitatory circuits as they also receive inputs from cones via bipolar cells (Chapot et al., 2017). Instead, the spatial, temporal, and gain modifications were greater in inhibitory inputs, which could not be mimicked by partial cone stimulation in the control retina. Furthermore, the density of inhibitory synapses increased on both bipolar cell axons and ganglion cell dendrites, and such structural changes were reflected functionally in the increased frequency of spontaneous inhibitory synaptic inputs to A_{ON-S} ganglion cells. We speculate that there are three possible mechanisms underlying the increase in inhibition.

First, since excitatory bipolar cells also provide inputs to inhibitory pathways, amacrine cells exhibiting increased synaptic output to bipolar and ganglion cells could receive excitatory input from bipolar cells that are either resilient or that recover from cone loss. Potential evidence for this includes the X (Shen et al., 2020) and S (Beier et al., 2018) bipolar cells that were previously shown to regain cone contacts in the mature retina following cone ablation, yet the functional output of these bipolar cells after dendritic remodeling remains unknown. Potential evidence against a resilient excitatory input to the amacrine cell from ON pathways includes a narrower excitatory center (Figure S2), a diminished excitatory gain (Figure 2), a lower frequency of mEPSCs (Figure 6), and a diminished ON cone bipolar-mediated b-wave in the ERG compared with the cone-mediated a-wave (Figure S4 in Care et al., 2019). These results indicate that synaptic outputs from ON cone bipolar cells were ubiquitously decreased after partial cone loss. In considering the resilient excitatory input to amacrine cells from OFF pathways, the excitatory gain from two types of OFF ganglion cells, which collectively receive input from 4 of the 5 types of OFF cone bipolar cells, was lower in cone-DTR retina (data not shown), suggesting a similar decrease in synaptic outputs from OFF cone bipolar cells. Taken together, a preserved bipolar cell input to the amacrine cell remains as a unique possibility.

A second possible mechanism involves serial inhibition of the amacrine cell(s) directly synapsing with the type 6 ON cone bipolar cell and A_{ON-S} ganglion cell. If the amacrine cell that provides direct input to the cells we examined receives less synaptic input from another upstream amacrine cell because of diminished excitatory output from a bipolar cell, then inhibitory currents might be amplified and prolonged. A similar phenomenon was reported in excitatory currents when presynaptic inhibition from amacrine cells to ON cone bipolar cells was diminished by elimination of the $GABA_A$ receptor (Nagy et al., 2021). Future studies will elucidate the role of serial inhibition to the changes in spatial and temporal processing.

Finally, a third mechanism that could explain the increased temporal integration of inhibition may be related to inhibitory receptor properties. We speculate that the insertion of new receptors may have subunits that are dominant during development. For example, developmental $GABA_A$ receptors contain the α3 subunit, which confers slower kinetics, as opposed to the α1 subunit, which confers faster kinetics in mature $GABA_A$ receptors (Barberis et al., 2007; Bosman et al., 2002; Sinha et al., 2021). Consistent with the increased temporal integration of inhibitory inputs, mIPSCs of A_{ON-S} ganglion cells in cone-DTR retina display slower decay time constants (data not shown). While the relative difference in time constants between control and cone-DTR is less than that in single channels exclusively containing either GABAα1 and α3 subunits (Barberis et al., 2007; Bosman et al., 2002; Gingrich et al., 1995; Vicini et al., 2001), our results may be consistent with the recruitment of a subset of $GABA_A$α3-containing receptors.

The three mechanisms we speculate about here could all contribute to the observed upregulation of inhibition. Further, we cannot rule out the possible contributions of horizontal cell feedback to the changes in spatial and temporal integration. Future experiments assessing horizontal cell feedback to cones will determine its potential contributions to surround expansion in excitatory input currents to the ganglion cell.

Regardless of a potential contribution from a unique bipolar cell, the structural and functional modifications in the inner retina provide another potential example of the greater remodeling capacity of inhibitory circuits. Perhaps with such a mild perturbation that ablates 50% to 60% of cones and less than 2% of the total photoreceptors in mouse retina, inhibitory circuits are better poised to make subtle modifications to the direct excitatory pathways without disrupting the overall fundamental processing goals of the circuit.

This study demonstrates that retinal circuits differentially react to partial cone loss and partial light stimulation. Only partial cone loss causes excitatory and inhibitory circuits to undergo distinctive functional and structural modifications, resulting in an enhancement of inhibitory synapses, a recovery of inhibitory response gain, and an expansion of receptive field surrounds, which together potentially preserve perception. Our findings provide mechanistic insights into how fundamental computations of the retina are maintained with fewer sensory inputs.

Limitations of the study

We acknowledge several limitations. First, these results are limited to acute cone death. How these results apply to conditions with more prolonged cell death, e.g., progressive or developmental, remains unknown. Second, we have focused on the circuits of a single ganglion cell type with limited evidence from a second type (Figure 1), leaving open the possibility that each ganglion cell type has a unique reaction to partial cone loss. Third, while we have localized synaptic changes at the level of inhibitory synapses onto bipolar and ganglion cells, we have not identified amacrine cell(s) or the underlying circuit responsible for the resilience or upregulation (Figure 5). Fourth, we have not directly tested the contributions from horizontal cells. Finally, we acknowledge the limitations of the image analysis (Figure 7), e.g., the perceptually based metric models the human visual system, and its relevance to the mouse remains to be tested.

STAR★METHODS

RESOURCE AVAILABILITY

Lead contact—Further information and requests for resources and reagents should be directed to and will be fulfilled by the lead contact, Felice Dunn (Felice.Dunn@ucsf.edu).

Material availability—This study did not generate new unique reagents.

Data and code availability

- All data reported in this paper will be shared by the lead contact upon request.
- All original code for the image analysis has been deposited at Github and is publically available as of the date of publication. The information is listed in the key resources table.
- Any additional information required to reanalyze the data reported in this paper is available from the lead contact upon request.

EXPERIMENTAL MODEL AND SUBJECT DETAILS

Mice—All procedures were done in accordance with the University of California, San Francisco Institutional Animal Care and Use protocols. Animals were maintained on a 12 h dark-12 h light cycle and fed standard mouse diet ad libitum. The following transgenic mouse lines were crossed: *OPN1SW-Cre* (Akimoto et al., 2004) for Cre-recombinase expression in short wavelength sensitive (S)-opsin or *OPN1MW-Cre* (Le et al., 2004) for Cre-recombinase expression in middle wavelength sensitive (M)-opsin, with *Rosa26-loxP-*

stop-loxP-DTR (Buch et al., 2005) for Cre-dependent expression of diphtheria toxin receptor (DTR), and *Grm6-TdTomato* for visualization of a sparse population of ON bipolar cells (Kerschensteiner et al., 2009). All transgenic mice were backcrossed into the *C57BL/6J* background. Male and female mice were used for experiments.

METHOD DETAILS

Diphtheria toxin induced cone death—To induce cone death, two intramuscular diphtheria toxin injections were made between P30–40, 7 days apart at dosages of 100 ng/g for *OPN1SW-Cre* and 50 ng/g for *OPN1MW-Cre* (Care et al., 2019). Mice injected with an equivalent volume of saline were used as littermate controls. The control condition is distinct from the DT-injected DTR-negative mice, used previously (Care et al., 2019).

Tissue preparation for immunostaining—Isolated dorsal-nasal retina was used for immunostaining with protocols identical to those described previously (Care et al., 2019). Only dorsal-nasal retina was used for imaging for consistency in cone distributions and ganglion cell sizes. Specific reagents used in this study are listed in the Key Resources Table.

Image acquisition—In the *Grm6-TdTomato* line, fluorescently-labeled type 6, 7, 8 cone bipolar cells were identified by their distinct axonal morphology and stratification in the inner plexiform layer (Dunn and Wong, 2012). Isolated bipolar cells and their associated synaptic puncta were imaged on a Leica SP8 confocal microscope using a 63×1.4 numerical aperture (NA) oil-immersion objective. Image stacks were acquired with a voxel size of 0.102 μm (x axis, y axis) and 0.3 μm (z axis). Each plane was acquired 2 times to obtain the average. Stacks of the entire inner plexiform layer labeled with synaptic puncta were acquired at resolution of 0.09 × 0.09 × 0.3 μm. Individual dye-filled A_{ON-S} ganglion cells were localized using epifluorescence and their dendrites and associated synaptic puncta were imaged with the following settings: 40x (1.3 NA) objective at resolution of 0.102× 0.102 × 0.3 μm.

Electrophysiology tissue preparation—Procedures for patch-clamp recording of A_{ON-S} and A_{OFF-S} ganglion cells in flat mount retina were identical to those described previously (Care et al., 2019, 2020). For bar noise stimuli (Figures 1, 2, 4), recordings were made in dorsal-nasal retina where the largest A_{ON-S} and A_{OFF-S} ganglion cells reside (Bleckert et al., 2014) and where middle (M)-wavelength sensitive opsin dominates (Applebury et al., 2000). For LED flashes (Figures 3E–3K), recordings were made in ventral-nasal retina where A_{ON-S} ganglion cells are large and where short (S)-wavelength sensitive opsin dominates. Following recordings, retinas were mounted on filter paper, fixed in 2% paraformaldehyde for 20 min, and processed for immunostaining.

Patch-clamp recordings—Patch electrodes were pulled from borosilicate glass (Sutter instruments) on a Narishige puller to 3–6 MOhm resistance. Under infrared light (950 nm), large polygonal somas were targeted as putative A_{ON-S} ganglion cells and large round somas were targeted as putative A_{OFF-S} ganglion cells. To type cells, extracellular spikes were recorded with an electrode filled with HEPES-buffered Ames in cell-attached configuration.

$A_{ON\text{-}S}$ ganglion cells were identified by their characteristically sustained spiking response to a 500 ms light step. $A_{OFF\text{-}S}$ ganglion cells were identified by their characteristically sustained spiking before and after a 500 ms light step. Extracellular recordings of spike responses to flashes were obtained for Figures 3E–3G. Once the identity of the ganglion cell was confirmed, a new electrode was used to make an intracellular recording. Whole-cell recordings were made with an electrode filled with an internal solution containing either potassium aspartate for current-clamp recordings (Figures 1, 3A–3D, S3 and S5) Care et al. (2020) or cesium methane sulfonate for voltage-clamp and current-clamp recordings when acquired in the same cell (Figures 2, 3H–3J, 4, 6, S2 and S4A–S4F) (Care et al., 2019) and 0.04% Lucifer yellow dye or 0.5% biocytin. Signals were amplified using an Axopatch MultiClamp 700B amplifier (Molecular Devices, Palo Alto, CA), digitized with an Instrutech ITC-18, and acquired with Symphony. After recordings, the identity of $A_{ON\text{-}S}$ and $A_{OFF\text{-}S}$ ganglion cells were further confirmed after immunostaining and imaging their dendritic morphology and stratification.

Light stimuli—To elicit spike responses for cell identification, a 470 nm LED was used to deliver a uniform spot of 2000 μm diameter for 500 ms. This wavelength was used to preferentially stimulate rods between the ranges of 8–400 photoisomerizations per rod per sec (Rh*/rod/sec). To measure the spatiotemporal receptive field profiles (Figures 1, 2, 4), a digital light projector (Lightcrafter Texas Instruments DLPLCR4500EVM) was used to deliver the bar noise stimulus. The projector image was generated by red, green, blue LEDs (420–700 nm) that preferentially stimulate M opsin rather than S opsin (Wang et al., 2011). The bar noise stimulus consisted of flickering bars (width of 40 μm; length of 1000 μm) with varying intensities randomly drawn from a Gaussian distribution and with mean intensity of 8,400 Rh*/rod/sec and standard deviation 0.3. Stimuli were presented for a total of at least 150 s. For the measurements of intrinsic excitability (Figure 3), to obtain cone-mediated responses, 10 ms flashes of a 370 nm LED that doubled intensities from 1.5 to 1300 photoisomerizations (P*)/S-cone were delivered on a mean background of 4000Rh*/rod/sec with a 470 nm LED to adapt the rods. To measure mini postsynaptic currents under the regime of cones (Figure 6), a mean background of 4000 Rh*/rod/sec with a 470 nm LED was used to adapt the rods.

Current injection—For current injection experiments, procedures were identical to those described in Care et al., 2020, with the addition of background light applied during the current injection. To place the retinal circuit in a resting state at which the cone circuitry dominates, we added a mean of 4000Rh*/rod/sec to adapt the rods before current injections. In a perforated patch-clamp configuration and a potassium aspartate internal solution, white noise current was injected for 40 sec for 6 repeats or more.

Spontaneous miniature postsynaptic currents—Spontaneous postsynaptic currents were recorded in voltage-clamp for a total of 10 min. Since each rod has a spontaneous isomerization rate of 0.012 Rh*/rod/sec (Baylor et al., 1979; Burns et al., 2002), and each $A_{ON\text{-}S}$ ganglion cell receives input from approximately 10,000 rods (Sterling et al., 1988; Takeshita et al., 2017; Tsukamoto et al., 2001), the estimated spontaneous event rate in darkness would be 120/sec. Gap junctions between ON cone bipolar cells via the

AII amacrine network would increase this spontaneous event rate. Riding on top of the fluctuations associated with spontaneous isomerizations are the single vesicle events we were trying to isolate. If each single vesicle event is approximately 12pA in amplitude and 10msec in duration, this spontaneous rate would cause single vesicle events arriving at random intervals to be difficult to discern from the larger and slower fluctuations caused by spontaneous isomerizations. Thus, to isolate individual excitatory events from the ON cone bipolar cell to the ganglion cell, we found that a combination of a sub-saturating concentration of the mGluR6 agonist 2-amino-4-phosphonobutyric acid (1μM APB) and a mean background that adapts the rods (4000Rh*/rod/sec) decreased the spontaneous isomerization rate sufficiently to detect individual vesicle events. In previous studies, mEPSCs in ganglion cells were recorded under room lights after isolated retinas had been incubated for 18–24 h (Morgan et al., 2008), therefore the spontaneous isomerization rates from bleached rods would be unlikely to obscure the measurement of single events under such conditions. For inhibitory postsynaptic currents, individual events could be isolated easily under the rod saturating background so that amacrine cell inputs that are most active under cone-light levels could be isolated.

Electroretinogram recordings—Analysis of electroretinogram recordings (ERG) were done on data previously acquired (Care et al., 2019).

Quantification of synaptic density—To quantify synaptic puncta associated with specific cell types, we used confocal images of type 2 bipolar cells labeled by immunostaining for Syt2 in the OFF sublamina, individual type 6–8 bipolar cell axons labeled in the *Grm6-TdTomato* line (Care et al., 2019; Dunn and Wong, 2012), and individual ganglion cells filled during physiology experiments. To determine gephyrin and VIAAT puncta distribution on the dendrites of individual A_{ON-S} ganglion cells, we modified a semiautomated method for quantifying synapse density as previously described (Della Santina et al., 2013; Morgan et al., 2011). ImageJ was used to median filter the images to remove thermal noise generated by the microscope’s detectors. Imaris was used to generate a 3-dimensional dendritic skeleton of the ganglion cell. Custom-written MATLAB routines were used to create a binary mask and used as a criteria to include gephyrin or VIAAT that exceeds 50% overlap with a mask. For bipolar cells, we created a binary mask of the axons of interest (Amira) and VolumeCut was used to select the OFF sublamina labeling of Syt2 within the IPL. Synaptic puncta associated with bipolar cell axons and A_{ON-S} ganglion cell dendrites were identified and manually validated in Object Finder with methods previously described (Della Santina et al., 2013). Linear puncta density was calculated within a moving window of 10 μm along the dendritic skeleton, starting from the cell soma. To directly map the location of peak puncta density from the ganglion cell dendrites to the corresponding depth in the inner plexiform layer (IPL), the following conversion was done. Based on previous serial electron micrograph reconstructions (Helmstaedter et al., 2013), A_{ON-S} ganglion cell dendrites were found to stratify between the innermost portion of the IPL (65%) and the end of the ON sublamina (100%). The peak location of synaptic puncta within each ganglion cell was normalized to IPL depth. This normalization allowed for A_{ON-S} ganglion cells dendrites of slightly varying sizes to be analyzed on the common reference of IPL depth.

QUANTIFICATION AND STATISTICAL ANALYSIS

Quantification of cone numbers—Procedure for counting cones, labeled either by cone arrestin or peanut agglutinin, were identical to those described previously (Care et al., 2019).

Analysis of the linear-nonlinear model—Spatiotemporal receptive fields from spikes first involved the isolation of spikes from the subthreshold voltages (Figures 1, S3 and S5). From intracellular current-clamp recordings of A_{ON-S} ganglion cells, spikes were isolated by the following criteria: voltages that exceeded (1) a threshold for spiking and (2) the absolute values of thresholds in the first (dVm/dt) and second (d^2Vm/d^2t) derivatives (Ozuysal and Baccus, 2012). Subthreshold voltages were interpolated using a smoothing spline interpolation at the times of the extracted spikes. Spike-triggered averaging of the stimulus and membrane-weighted averaging of the stimulus were used to compute linear receptive fields for isolated spikes and subthreshold voltages, respectively. Procedures for measuring the spatiotemporal receptive fields from subthreshold voltages, excitatory currents, and inhibitory currents were identical to those described previously (Care et al., 2019). As in the previous work, we normalized the linear filter such that it was a unit vector. This choice of normalization places all gain information into the nonlinearity. In response to the bar noise stimulus, linear spatial receptive fields were used to measure the following parameters: one standard deviation center width, one standard deviation surround width, and center-to-surround amplitude ratio (Figures 1 and S2). The linear filter was also used to measure temporal information. A single temporal linear filter was measured by projecting the linear filters from each region of space along the first principal component measured across all filters. That single temporal linear filter was used to measure the time-to-peak and integration time of the ganglion cell responses (Figures 4, S4 and S5). Integration time was calculated as the integral of responses divided by the peak amplitudes.

The nonlinear component of the model maps the convolution of the linear filter and stimulus to the cell's response, i.e., voltage, excitatory current, or inhibitory current (Figures 2 and S3). From the nonlinearity, the cell's gain was measured as the slope of a line of best fit (Appleby and Manookin, 2019; Kim and Rieke, 2001; Nagy et al., 2021; Ozuysal et al., 2018). We quantified the root mean squared (RMS) error of the linear fit and the entire curve and found that the error is similar in all conditions, i.e., the nonlinearity deviates from a linear fit equally across conditions (RMS error for spikes, control: 3.89 ± 0.32, cone-DTR: 4.89 ± 0.43, $p = 0.12$; RMS for voltage, control: 0.69 ± 0.02, cone-DTR: 0.74 ± 0.01, $p = 0.06$; RMS error for excitation, control: 9.61 ± 0.13, cone-DTR: 9.84 ± 0.12, $p = 0.86$; RMS error for inhibition, control: 2.76 ± 0.04, cone-DTR: 2.28 ± 0.06, $p = 0.09$, mean ± SEM, rank sum). Only cells with linear spatial filters that could be fit by the difference of Gaussians model (Care et al., 2019) were used in analysis of the gain. Ganglion cells whose receptive field could not be fit with a difference of Gaussians were excluded from the population analysis and comprised 29% (48 of 161) of recorded ganglion cells in cone-DTR retina. This criterion was chosen to eliminate ganglion cells in both control and cone-DTR that did not respond robustly to the bar noise stimulus.

The linear-nonlinear model was also used in the current injection analysis (Figures 3A–3D). The time-reversed spike-triggered average of the injected current represents the linear filter. The nonlinear filter is plotted with the abscissa as the convolution between the spike-triggered average and the stimulus in units of standard deviation against the ordinate, which is the spike rate (Figure 3D). The nonlinearity for each cell was interpolated and smoothed with a spline function before calculating the average.

Quantification of intensity-response relationships—To analyze maximum spike response or peak current to flash families, the averages of each response were fit with the Hill equation in Igor Pro as described previously (Care et al., 2020),

$$\text{fit} = \text{base} + \frac{R_{\text{max}} - \text{base}}{1 + \left[\frac{X_{\text{half}}}{X}\right]^{\text{rate}}}$$

where base is the minimum response, R_{max} is the maximum value of the curve, rate is the inverse of the slope of the curve, and X_{half} is the intensity at the half maximum (referred as $I_{1/2}$ in Figures 3F, 3I and Table S3).

Mini analysis—Detection of mEPSCs and mIPSCs were performed using TaroTools in Igor Pro (Ishikawa et al., 2015). Data were low pass filtered at 100 Hz. Filtered data were thresholded by 1.5 times the standard deviation to limit inclusion of false-positive events. Postsynaptic events selected by the threshold were validated empirically. Isolated waveform clusters were further validated by a custom-written MATLAB code using principal component analysis to extract a main cluster and exclude outliers. Mean amplitude and frequency of synaptic events were then calculated based on the remaining isolated postsynaptic events.

Image analysis—3D receptive fields were generated by revolving average linear spatial filters from (1) full and (2) partial stimulation of control, and (3) cone-DTR retinas. Each of the three spatial filters across a range of image sizes 4000, 2000, 400, and 200 times the receptive field pixel size were used for convolving a reference image. Such a convolution was done on 148 natural images. The mean squared error (MSE) and structural similarity index (SSIM) was used to quantify the difference between convolved images with the reference image as a function of image-to-receptive field pixel ratios.

Statistical analysis—Data are represented as median ± interquartile range (IQR) in Figures 1, 2, 3G, 3J, 3K, 4, 5D–5F, and 6, and as mean ± sem in Figures 3C, 3D, 5I–5K, 5N–5P (line and shaded region), and 7. A Wilcoxon rank-sum test (abbr. rank sum) was used to determine significant differences between control and cone-DTR conditions. A Wilcoxon sign rank test (abbr. sign rank) was used to determine significant differences between control full stimulation and control half stimulation conditions because these data were acquired within the same ganglion cells. A two-way ANOVA test was used to determine significant differences between convolved images with the reference image. The following asterisks in the figures indicate p values: $^* \leq 0.05$, $^{**} \leq 0.01$, $^{***} \leq 0.005$.

Supplementary Material

Refer to Web version on PubMed Central for supplementary material.

ACKNOWLEDGMENTS

We thank Connie Chen and Jeremiah John for technical assistance, Scott Harris, Mrinalini Hoon, Jeanette Hyer, Yvonne Ou, Manuel Solino, and Alfred Yu for helpful discussions, Jae Lee for providing natural images, and Fred Rieke for helpful comments. This work was supported by NIH through the Vision Core Grants P30 EY002162 (UCSF) and EY029772 (F.A.D.) and by foundation grants from McKnight Scholar Award, Research to Prevent Blindness Unrestricted Grant, and That Man May See.

REFERENCES

Akimoto M, Filippova E, Gage PJ, Zhu X, Craft CM, and Swaroop A (2004). Transgenic mice expressing Cre-recombinase specifically in M- or S-cone photoreceptors. Investig. Opthalmol. Vis. Sci 45, 42.

Applebury ML, Antoch MP, Baxter LC, Chun LL, Falk JD, Farhangfar F, Kage K, Krzystolik MG, Lyass LA, and Robbins JT (2000). The murine cone photoreceptor: a single cone type expresses both S and M opsins with retinal spatial patterning. Neuron 27, 513–523. [PubMed: 11055434]

Appleby TR, and Manookin MB (2019). Neural sensitization improves encoding fidelity in the primate retina. Nat. Commun 10, 4017. [PubMed: 31488831]

Atick JJ, and Redlich AN (1990). Towards a theory of early visual processing. Neural Comput. 2, 308–320.

Baccus SA, and Meister M (2002). Fast and slow contrast adaptation in retinal circuitry. Neuron 36, 909–919. [PubMed: 12467594]

Barberis A, Mozrzymas JW, Ortinski PI, and Vicini S (2007). Desensitization and binding properties determine distinct $\alpha 1\beta 2\gamma 2$ and $\alpha 3\beta 2\gamma 2$ GABAA receptor-channel kinetic behavior: kinetics of $\alpha 1\beta 2\gamma 2$ and $\alpha 3\beta 2\gamma 2$ channels. Eur. J. Neurosci 25, 2726–2740. [PubMed: 17561840]

Barlow HB, Fitzhugh R, and Kuffler SW (1957). Change of organization in the receptive fields of the cat's retina during dark adaptation. J. Physiol 137, 338–354. [PubMed: 13463771]

Baylor DA, Lamb TD, and Yau KW (1979). Responses of retinal rods to single photons. J. Physiol 288, 613–634. [PubMed: 112243]

Beier C, Palanker D, and Sher A (2018). Stereotyped synaptic connectivity is restored during circuit repair in the adult mammalian retina. Curr. Biol 28, 1818–1824.e2. [PubMed: 29804805]

Bleckert A, Schwartz GW, Turner MH, Rieke F, and Wong ROL (2014). Visual space is represented by non-matching topographies of distinct mouse retinal ganglion cell types. Curr. Biol 24, 310–315. [PubMed: 24440397]

Borghuis BG, Ratliff CP, and Smith RG (2018). Impact of light-adaptive mechanisms on mammalian retinal visual encoding at high light levels. J. Neurophysiol 119, 1437–1449. [PubMed: 29357459]

Bosman LWJ, Rosahl TW, and Brussaard AB (2002). Neonatal development of the rat visual cortex: synaptic function of GABAA receptor alpha subunits. J. Physiol 545, 169–181. [PubMed: 12433958]

Buch T, Heppner FL, Tertilt C, Heinen TJAJ, Kremer M, Wunderlich FT, Jung S, and Waisman A (2005). A Cre-inducible diphtheria toxin receptor mediates cell lineage ablation after toxin administration. Nat. Methods 2, 419–426. [PubMed: 15908920]

Burns ME, Mendez A, Chen J, and Baylor DA (2002). Dynamics of cyclic GMP synthesis in retinal rods. Neuron 36, 81–91. [PubMed: 12367508]

Care RA, Kastner DB, De la Huerta I, Pan S, Khoche A, Della Santina L, Gamlin C, Santo Tomas C, Ngo J, Chen A, et al. (2019). Partial cone loss triggers synapse-specific remodeling and spatial receptive field rearrangements in a mature retinal circuit. Cell Rep. 27, 2171–2183.e5. [PubMed: 31091454]

Care RA, Anastassov IA, Kastner DB, Kuo Y-M, Della Santina L, and Dunn FA (2020). Mature retina compensates functionally for partial loss of rod photoreceptors. Cell Rep. 31, 107730. [PubMed: 32521255]

Chapot CA, Euler T, and Schubert T (2017). How do horizontal cells 'talk' to cone photoreceptors? Different levels of complexity at the cone-horizontal cell synapse: how do horizontal cells 'talk' to cone photoreceptors? J. Physiol 595, 5495–5506. [PubMed: 28378516]

Chen JL, Villa KL, Cha JW, So PTC, Kubota Y, and Nedivi E (2012). Clustered dynamics of inhibitory synapses and dendritic spines in the adult neocortex. Neuron 74, 361–373. [PubMed: 22542188]

Della Santina L, Inman DM, Lupien CB, Horner PJ, and Wong ROL (2013). Differential progression of structural and functional alterations in distinct retinal ganglion cell types in a mouse model of Glaucoma. J. Neurosci 33, 17444–17457. [PubMed: 24174678]

Della Santina L, Yu AK, Harris SC, Soliño M, Garcia Ruiz T, Most J, Kuo Y-M, Dunn FA, and Ou Y (2021). Disassembly and rewiring of a mature converging excitatory circuit following injury. Cell Rep. 36, 109463. [PubMed: 34348156]

Demb JB, Haarsma L, Freed MA, and Sterling P (1999). Functional circuitry of the retinal ganglion cell's nonlinear receptive field. J. Neurosci 19, 9756–9767. [PubMed: 10559385]

Demb JB, Zaghloul K, Haarsma L, and Sterling P (2001). Bipolar cells contribute to nonlinear spatial summation in the Brisk-Transient (Y) ganglion cell in mammalian retina. J. Neurosci 21, 7447–7454. [PubMed: 11567034]

Dunn FA, and Wong ROL (2012). Diverse strategies engaged in establishing stereotypic wiring patterns among neurons sharing a common input at the visual system's first synapse. J. Neurosci 32, 10306–10317. [PubMed: 22836264]

Eavri R, Shepherd J, Welsh CA, Flanders GH, Bear MF, and Nedivi E (2018). Interneuron simplification and loss of structural plasticity as markers of aging-related functional decline. J. Neurosci 38, 8421–8432. [PubMed: 30108129]

Eggers ED, and Lukasiewicz PD (2011). Multiple pathways of inhibition shape bipolar cell responses in the retina. Vis. Neurosci 28, 95–108. [PubMed: 20932357]

Enroth-Cugell C, and Robson JG (1966). The contrast sensitivity of retinal ganglion cells of the cat. J. Physiol 187, 517–552. [PubMed: 16783910]

Freeman J, Field GD, Li PH, Greschner M, Gunning DE, Mathieson K, Sher A, Litke AM, Paninski L, Simoncelli EP, et al. (2015). Mapping nonlinear receptive field structure in primate retina at single cone resolution. Elife 4, e05241. [PubMed: 26517879]

Gingrich KJ, Roberts WA, and Kass RS (1995). Dependence of the GABAA receptor gating kinetics on the alpha-subunit isoform: implications for structure-function relations and synaptic transmission. J. Physiol 489, 529–543. [PubMed: 8847645]

Helmstaedter M, Briggman KL, Turaga SC, Jain V, Seung HS, and Denk W (2013). Connectomic reconstruction of the inner plexiform layer in the mouse retina. Nature 500, 168–174. [PubMed: 23925239]

Hsu W-MM, Kastner DB, Baccus SA, and Sharpee TO (2021). How inhibitory neurons increase information transmission under threshold modulation. Cell Rep. 35, 109158. [PubMed: 34038717]

Ishikawa T, Shimuta M, and Häusser M (2015). Multimodal sensory integration in single cerebellar granule cells in vivo. Elife 4, e12916. [PubMed: 26714108]

Kastner DB, and Baccus SA (2011). Coordinated dynamic encoding in the retina using opposing forms of plasticity. Nat. Neurosci 14, 1317–1322. [PubMed: 21909086]

Kastner DB, and Baccus SA (2014). Insights from the retina into the diverse and general computations of adaptation, detection, and prediction. Curr. Opin. Neurobiol 25, 63–69. [PubMed: 24709602]

Kastner DB, Baccus SA, and Sharpee TO (2015). Critical and maximally informative encoding between neural populations in the retina. Proc. Natl. Acad. Sci 112, 2533–2538. [PubMed: 25675497]

Kerschensteiner D, Morgan JL, Parker ED, Lewis RM, and Wong ROL (2009). Neurotransmission selectively regulates synapse formation in parallel circuits in vivo. Nature 460, 1016–1020. [PubMed: 19693082]

Kim KJ, and Rieke F (2001). Temporal contrast adaptation in the input and output signals of salamander retinal ganglion cells. J. Neurosci 21, 287–299. [PubMed: 11150346]

Krieger B, Qiao M, Rousso DL, Sanes JR, and Meister M (2017). Four alpha ganglion cell types in mouse retina: function, structure, and molecular signatures. PLoS One 12, e0180091. [PubMed: 28753612]

Le Y-Z, Ash JD, Al-Ubaidi MR, Chen Y, Ma J-X, and Anderson RE (2004). Targeted expression of Cre recombinase to cone photoreceptors in transgenic mice. Mol. Vis 10, 1011–1018. [PubMed: 15635292]

Lee JY, Care RA, Della Santina L, and Dunn FA (2021). Impact of photoreceptor loss on retinal circuitry. Annu. Rev. Vis. Sci 7, 105–128. [PubMed: 34524879]

Margolis DJ, and Detwiler PB (2007). Different mechanisms generate maintained activity in ON and OFF retinal ganglion cells. J. Neurosci 27, 5994–6005. [PubMed: 17537971]

Morgan JL, Schubert T, and Wong RO (2008). Developmental patterning of glutamatergic synapses onto retinal ganglion cells. Neural Dev. 3, 8. [PubMed: 18366789]

Morgan JL, Soto F, Wong ROL, and Kerschensteiner D (2011). Development of cell type-specific connectivity patterns of converging excitatory axons in the retina. Neuron 71, 1014–1021. [PubMed: 21943599]

Murphy GJ, and Rieke F (2006). Network variability limits stimulus-evoked spike timing precision in retinal ganglion cells. Neuron 52, 511–524. [PubMed: 17088216]

Nagy J, Ebbinghaus B, Hoon M, and Sinha R (2021). GABAA presynaptic inhibition regulates the gain and kinetics of retinal output neurons. Elife 10, e60994. [PubMed: 33904401]

Okawa H, Della Santina L, Schwartz GW, Rieke F, and Wong ROL (2014). Interplay of cell-autonomous and nonautonomous mechanisms tailors synaptic connectivity of converging axons in vivo. Neuron 82, 125–137. [PubMed: 24698272]

Olshausen BA, and Field DJ (2005). How close are we to understanding V1? Neural Comput. 17, 1665–1699. [PubMed: 15969914]

Ozuysal Y, and Baccus SA (2012). Linking the computational structure of variance adaptation to biophysical mechanisms. Neuron 73, 1002–1015. [PubMed: 22405209]

Ozuysal Y, Kastner DB, and Baccus SA (2018). Adaptive feature detection from differential processing in parallel retinal pathways. PLoS Comput. Biol 14, e1006560. [PubMed: 30457994]

Park SJH, Pottackal J, Ke J-B, Jun NY, Rahmani P, Kim I-J, Singer JH, and Demb JB (2018). Convergence and divergence of CRH amacrine cells in mouse retinal circuitry. J. Neurosci 38, 3753–3766. [PubMed: 29572434]

Pfeiffer RL, Marc RE, and Jones BW (2020). Persistent remodeling and neurodegeneration in late-stage retinal degeneration. Prog. Retin. Eye Res 74, 100771. [PubMed: 31356876]

Saiepour MH, Chakravarthy S, Min R, and Levelt CN (2015). Competition and homeostasis of excitatory and inhibitory connectivity in the adult mouse visual cortex. Cereb. Cortex 25, 3713–3722. [PubMed: 25316336]

Schwartz GW, Okawa H, Dunn FA, Morgan JL, Kerschensteiner D, Wong RO, and Rieke F (2012). The spatial structure of a nonlinear receptive field. Nat. Neurosci 15, 1572–1580. [PubMed: 23001060]

Shen N, Wang B, Soto F, and Kerschensteiner D (2020). Homeostatic plasticity shapes the retinal response to photoreceptor degeneration. Curr. Biol 30, 1916–1926.e3. [PubMed: 32243858]

Sinha R, Grimes WN, Wallin J, Ebbinghaus BN, Luu K, Cherry T, Rieke F, Rudolph U, Wong RO, and Hoon M (2021). Transient expression of a GABA receptor subunit during early development is critical for inhibitory synapse maturation and function. Curr. Biol 31, 4314–4326.e5. [PubMed: 34433078]

Smeds L, Takeshita D, Turunen T, Tiihonen J, Westö J, Martyniuk N, Seppänen A, and Ala-Laurila P (2019). Paradoxical rules of spike train decoding revealed at the sensitivity limit of vision. Neuron 104, 576–587.e11. [PubMed: 31519460]

Sterling P, Freed MA, and Smith RG (1988). Architecture of rod and cone circuits to the on-beta ganglion cell. J. Neurosci 8, 623–642. [PubMed: 2828567]

Takeshita D, Smeds L, and Ala-Laurila P (2017). Processing of single-photon responses in the mammalian on and off retinal pathways at the sensitivity limit of vision. Philos. Trans. R. Soc. B Biol. Sci 372, 20160073.

Tien N-W, Soto F, and Kerschensteiner D (2017). Homeostatic plasticity shapes cell-type-specific wiring in the retina. Neuron 94, 656–665.e4. [PubMed: 28457596]

Tkačik G, Garrigan P, Ratliff C, Milčinski G, Klein JM, Seyfarth LH, Sterling P, Brainard DH, and Balasubramanian V (2011). Natural images from the birthplace of the human eye. PLoS One 6, e20409. [PubMed: 21698187]

Tsukamoto Y, and Omi N (2017). Classification of mouse retinal bipolar cells: type-specific connectivity with special reference to rod-driven AII amacrine pathways. Front. Neuroanat 11, 92. [PubMed: 29114208]

Tsukamoto Y, Morigiwa K, Ueda M, and Sterling P (2001). Microcircuits for night vision in mouse retina. J. Neurosci 21, 8616–8623. [PubMed: 11606649]

Van Hateren JH (1993). Spatiotemporal contrast sensitivity of early vision. Vis. Res 33, 257–267. [PubMed: 8447098]

van Hateren JH, Rüttiger L, Sun H, and Lee BB (2002). Processing of natural temporal stimuli by Macaque retinal ganglion cells. J. Neurosci 22, 9945–9960. [PubMed: 12427852]

van Versendaal D, Rajendran R, Saiepour MH, Klooster J, Smit-Rigter L, Sommeijer J-P, De Zeeuw CI, Hofer SB, Heimel JA, and Levelt CN (2012). Elimination of inhibitory synapses is a major component of adult ocular dominance plasticity. Neuron 74, 374–383. [PubMed: 22542189]

Van Wyk M, Wässle H, and Taylor WR (2009). Receptive field properties of ON- and OFF-ganglion cells in the mouse retina. Vis. Neurosci 26, 297–308. [PubMed: 19602302]

Vicini S, Ferguson C, Prybylowski K, Kralic J, Morrow AL, and Homanics GE (2001). GABA A receptor α1 subunit deletion prevents developmental changes of inhibitory synaptic currents in cerebellar neurons. J. Neurosci 21, 3009–3016. [PubMed: 11312285]

Villa KL, Berry KP, Subramanian J, Cha JW, Oh WC, Kwon H-B, Kubota Y, So PTC, and Nedivi E (2016). Inhibitory synapses are repeatedly assembled and removed at persistent sites in vivo. Neuron 89, 756–769. [PubMed: 26853302]

Wang Z, Bovik AC, Sheikh HR, and Simoncelli EP (2004). Image quality assessment: from error visibility to structural similarity. IEEE Trans. Image Process 13, 600–612. [PubMed: 15376593]

Wang YV, Weick M, and Demb JB (2011). Spectral and temporal sensitivity of cone-mediated responses in mouse retinal ganglion cells. J. Neurosci 31, 7670–7681. [PubMed: 21613480]

Warrant EJ (1999). Seeing better at night: life style, eye design and the optimum strategy of spatial and temporal summation. Vis. Res 39, 1611–1630. [PubMed: 10343855]

Weber AI, Krishnamurthy K, and Fairhall AL (2019). Coding principles in adaptation. Annu. Rev. Vis. Sci 5, 427–449. [PubMed: 31283447]

Highlights

- Inhibition, not excitation, endures cone loss with greater spatiotemporal integration
- Inhibition onto type 6 bipolar cell axons and $A_{ON\text{-}S}$ ganglion cell dendrites increases
- Frequency of synaptic release increases for inhibition and decreases for excitation
- Spatial filtering of static natural images is perceptually identical after cone loss

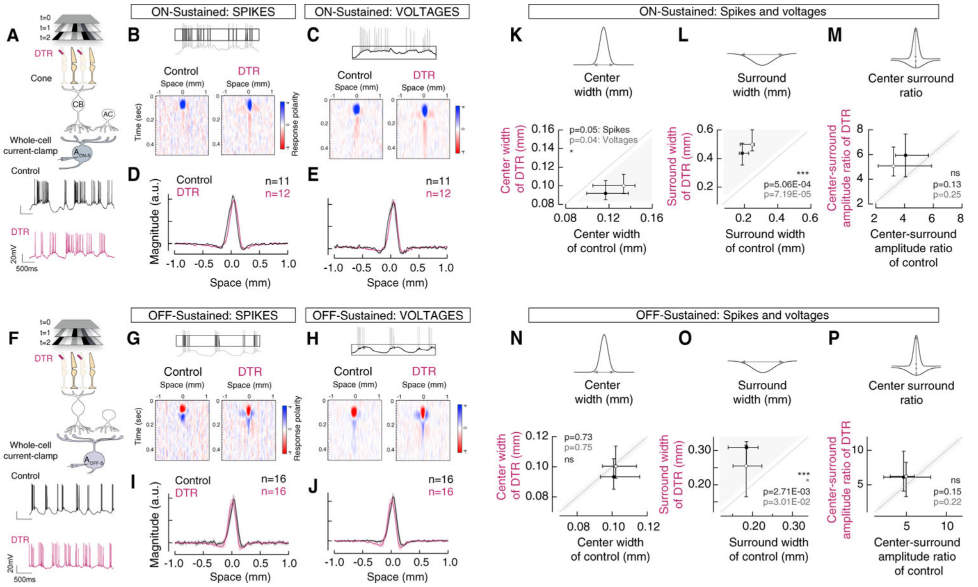

Figure 1. Increased surround widths of spatial receptive fields measured from spikes and subthreshold voltages of A_{ON-S} and A_{OFF-S} ganglion cells after partial cone loss

(A and F) Schematic of the bar noise stimulus presented to the retina after partial cone loss while recording spikes and subthreshold voltages from (A) A_{ON-S} and (F) A_{OFF-S} ganglion cells in whole-cell current clamp.

(B, C, G, and H) Spatiotemporal receptive fields from isolated (B and G) spikes and (C and H) subthreshold voltages from (B and C) A_{ON-S} and (G and H) A_{OFF-S} ganglion cells in control (left) and cone-DTR retina (right). (D, E, I, and J) Average spatial filters from (D and I) spikes and (E and J) subthreshold voltages. Line and shade represent mean ± SEM.

(K–M) Receptive field parameters from fits to a difference of Gaussians show A_{ON-S} with (K) significantly narrower one standard deviation (SD) center width, (L) significantly wider one SD surround width, and (M) no significant difference in the center-to-surround amplitudes between control and cone-DTR for both spikes (closed circles) and subthreshold voltages (open circles).

(N–P) A_{OFF-S} show (N) no significant differences in the one SD center width, (O) significantly wider one SD surround width, and (P) no significant difference in the center-to-surround amplitudes between control and cone-DTR for both spikes and subthreshold voltages.

Circles represent median ± interquartile range (IQR) across ganglion cells of each type. Gray indicates the region where medians reside. Line has unity slope. n represents the number of cells recorded. p values: * ≤ 0.05, ** ≤ 0.01, *** ≤ 0.005. CB, cone bipolar cell; AC, amacrine cell. Animal numbers listed in Table S1.

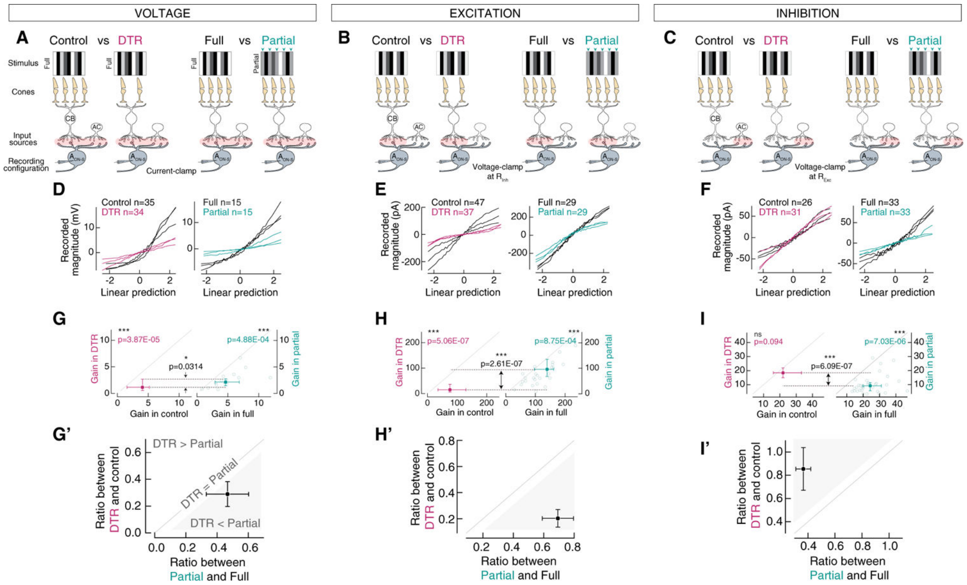

Figure 2. Gain of voltage and excitatory input responses diminish while gain of inhibitory inputs to $A_{ON\text{-}S}$ ganglion cells recover after partial cone loss

(A–C) Response gain measured from the nonlinearity of $A_{ON\text{-}S}$ ganglion cells to the bar noise stimuli in four conditions described by the stimuli (full versus partial, green arrowheads indicate bars held at a constant mean), cone numbers (control versus cone-DTR), input sources (excitation and/or inhibition, pink ovals), and recording configuration (current clamp or voltage clamp): (1) full stimulation of control retina, (2) full stimulation of cone-DTR retina, (3) another group of full stimulation of control retina, and (4) partial stimulation of control retina.

(D–F) Three exemplar nonlinearities for (D) voltages, (E) excitatory currents, and (F) inhibitory currents from individual $A_{ON\text{-}S}$ ganglion cells in control and cone-DTR retinas (left) and under full and partial stimulation of control retina (right).

(G and H) Gain, determined by the slope of a line fit to the nonlinearity, from (G) voltages and (H) excitatory currents were significantly lower in both cone-DTR (magenta) and partial stimulation of control (green) compared with in their respective control groups.

(I) Gain from inhibitory currents was indistinguishable in control and cone-DTR retinas; however, gain from inhibitory currents was significantly lower in partial stimulation compared with in full stimulation retina. Individual cells for paired conditions (open circles) and median ± IQR (closed circles ± error bars) in comparing paired full and partial stimulation of the same $A_{ON\text{-}S}$ ganglion cells in control retina and unpaired $A_{ON\text{-}S}$ ganglion cells in control and cone-DTR retinas.

(G′–I′) Gain difference between cone-DTR and partial stimulation is calculated by the ratios of the median gain from cone-DTR over control (ordinate) and from partial over full stimulation conditions (abscissa) represented by closed circles and error bars (median of ratios ± propagated ratio errors). Gray indicates the region where ratios reside (black p values in G–I).

Line has unity slope. n represents the number of cells recorded. p values: * ≤ 0.05, ** ≤ 0.01, *** ≤ 0.005.

See also Table S2.

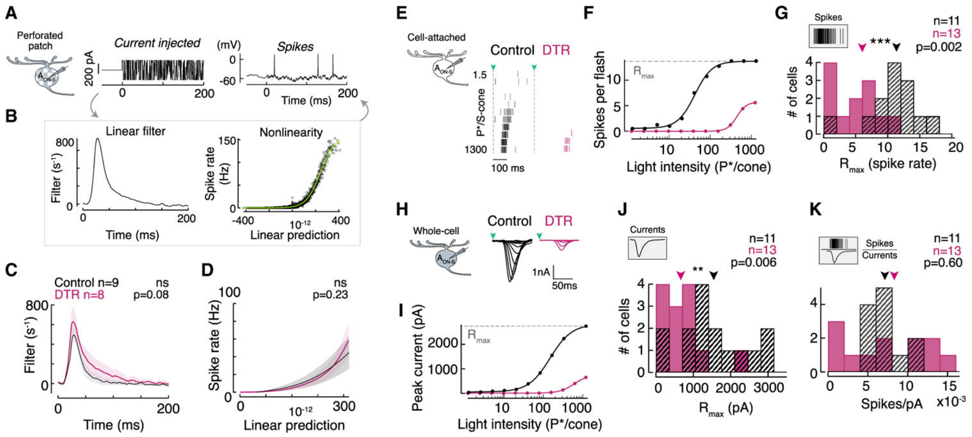

Figure 3. Intrinsic excitability of A_{ON-S} ganglion cells is maintained after partial cone loss

(A) A_{ON-S} ganglion cell recorded by perforated patch in which current was injected (left) and spikes were recorded (right) on a blue mean.

(B) Current-to-spike transformation is captured by a time-reversed spike-triggered average (left) and nonlinearity (right), which is fit with a sigmoid function (green).

(C and D) Average time-reversed spike-triggered averages (C) and average nonlinearity (D).

(E–H) Example A_{ON-S} ganglion cells' (E) cell-attached spikes and (H) voltage-clamped excitatory currents in response to a 10 ms UV flash doubling in intensity on top of a blue mean. Flashes were delivered at the time shown by the green arrow.

(F and I) Average intensity-response relationship for the (F) total number of spikes and (I) peak excitatory current in response to each light intensity from the cells in (E) and (H). Average intensity-response relationships represented by closed circles.

(G and J) Histograms of (G) spikes and (J) excitatory current maximum responses from Hill equation fits (R_{max}) for A_{ON-S} ganglion cells from control and cone-DTR retinas. Arrowheads indicate median.

(K) Histograms of the ratio between maximum spikes and currents from the Hill equation fits (R_{max}) measured in the same A_{ON-S} ganglion cells from control and cone-DTR retinas.

n represents the number of cells. p values: * ≤ 0.05, ** ≤ 0.01, *** ≤ 0.005.

See also Table S3.

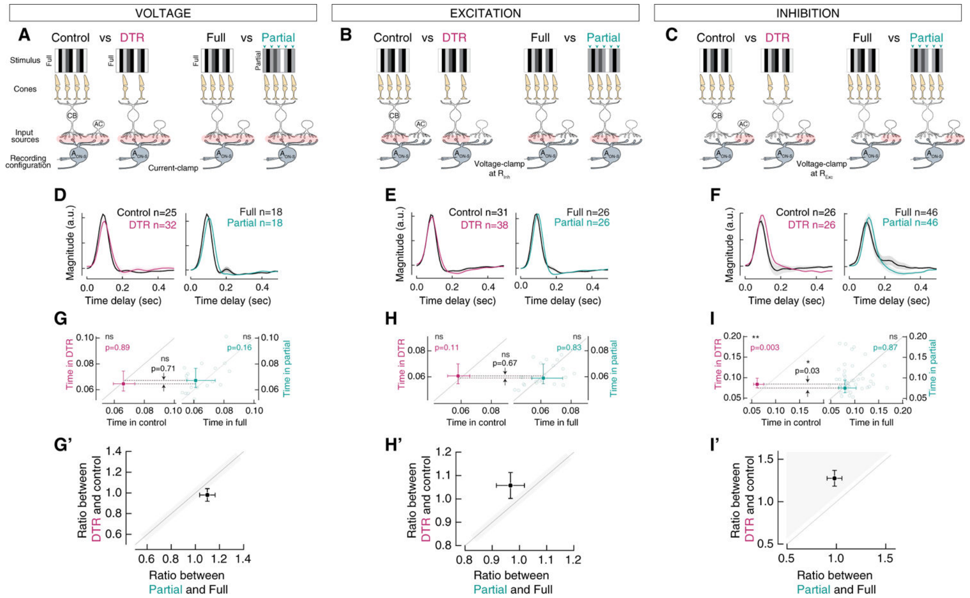

Figure 4. Greater integration time of inhibitory input currents in A_{ON-S} ganglion cells following partial cone loss

(A–C) Schematic of 4 conditions: (1) full stimulation of control retina, (2) full stimulation of cone-DTR retina, (3) another group of full stimulation of control retina, and (4) partial stimulation of control retina.

(D–F) Average temporal filters from A_{ON-S} ganglion cell (D) voltages, (E) excitatory currents, and (F) inhibitory currents for control and cone-DTR conditions (left) and under full and partial stimulation (right). Solid line and shade indicate mean ± SEM.

(G and H) Integration times of (G) voltage and (H) excitatory current filters were not significantly different in cone-DTR nor in the partial stimulation of control compared with in their respective control groups.

(I) Integration times of inhibitory responses were significantly greater in cone-DTR than in control retina; however, integration times of inhibitory responses were not significantly different between full and partial stimulation of the same control A_{ON-S} ganglion cell. Individual cells for paired conditions (open circles) and median ± IQR (closed circles ± error bars) in comparing paired full and partial stimulation of the same A_{ON-S} ganglion cells in control retina and unpaired A_{ON-S} ganglion cells in control and cone-DTR retinas.

(G′–I′) Integration time difference between cone-DTR and partial stimulation is calculated by the ratios between median integration times from cone-DTR over control (ordinate) and between partial over full stimulation conditions (abscissa) represented by closed circles and error bars (median of ratios ± propagated ratio errors). Gray indicates the region where the ratios reside (black p values in G–I).

Line has unity slope. n represents the number of cells recorded. p values: * ≤ 0.05, ** ≤ 0.01, *** ≤ 0.005.

See also Table S4.

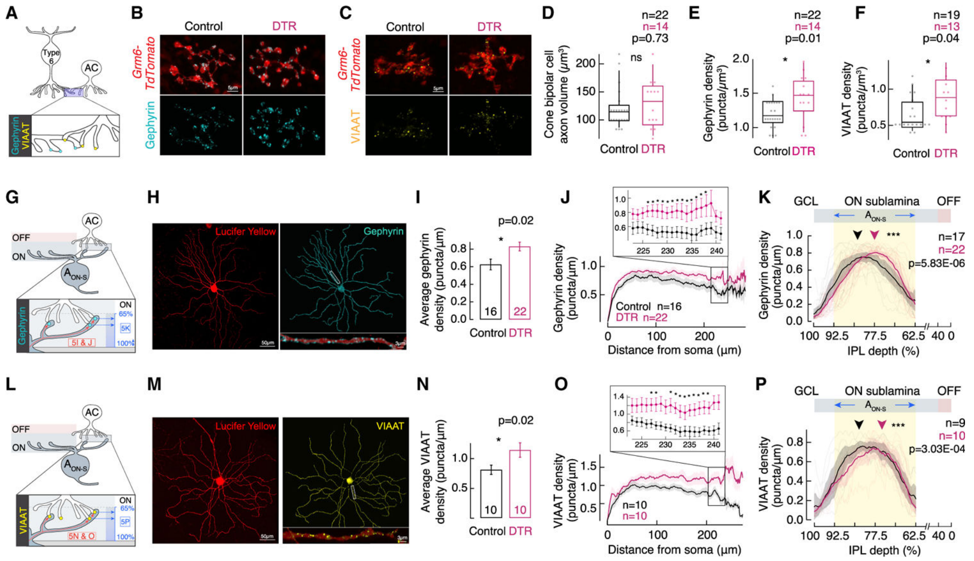

Figure 5. Densities of inhibitory receptors increase in type 6 cone bipolar cell axons and in A_{ON-S} ganglion cell dendrites after partial cone loss

(A) Schematic of amacrine cell input to type 6 ON cone bipolar cell axons with presynaptic VIAAT and postsynaptic gephyrin.

(B and C) *En face* confocal images of type 6 cone bipolar cell axons labeled in the *Grm6-TdTomato* line (red) with (B) gephyrin (cyan) and (C) apposing VIAAT (yellow) immunostaining.

(D) Volume of type 6 cone bipolar cell axons.

(E and F) Puncta density for (E) gephyrin within or (F) VIAAT apposed to each type 6 axon.

(G and L) Schematic of amacrine cell input to A_{ON-S} ganglion cell dendrites represented as (G) postsynaptic gephyrin or (L) presynaptic VIAAT. Box illustrates linear puncta density as a function of distance from the soma (red arrows; quantified in I–J and N–O) and as a function of the inner plexiform layer (IPL) depth (blue arrows; quantified in K and P).

(H and M) *En face* confocal images of a control A_{ON-S} ganglion cell filled with lucifer yellow (red) and immunostained with (H) gephyrin or (M) VIAAT. Insets show a stretch of dendrites with puncta for rectangles in main images.

(I and N) Average linear density of (I) gephyrin or (N) VIAAT with SEM.

(J and O) Linear density of (J) gephyrin or (O) VIAAT across the ganglion cell's dendrites from the soma (0) to periphery (300 μm). Box indicates eccentricities with significantly increased puncta density. Solid line and shade indicate mean ± SEM.

(K and P) Linear density of (K) gephyrin or (P) VIAAT across the IPL distance. Yellow shade depicts stratification of A_{ON-S} ganglion cell dendrites in conventionally defined IPL depth.

Cell numbers denoted in each panel. p values: * ≤ 0.05, ** ≤ 0.01, *** ≤ 0.005.

See also Table S5.

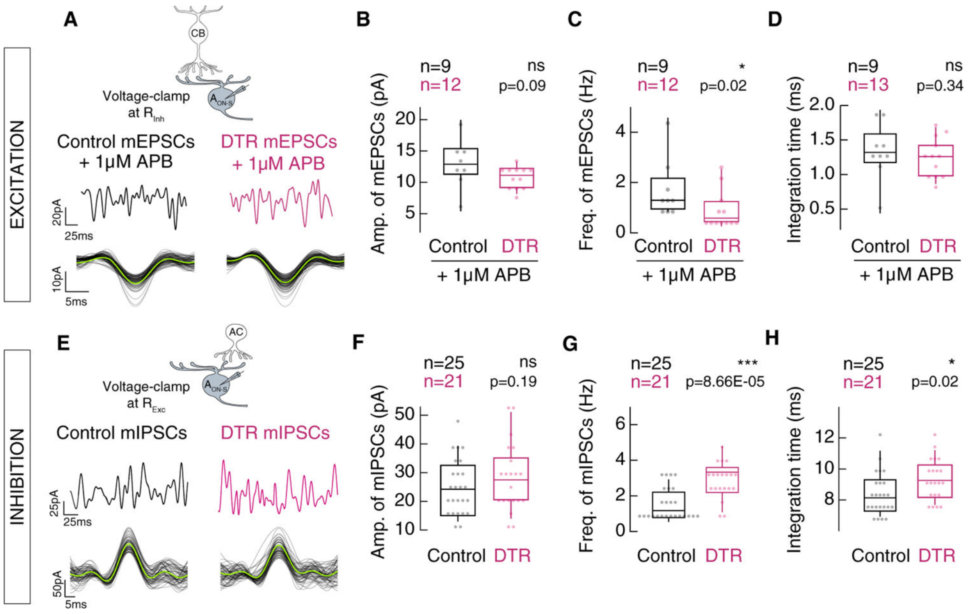

Figure 6. Frequencies of spontaneous miniature postsynaptic currents in A_{ON-S} ganglion cells decrease in excitation and increase in inhibition following partial cone loss

(A and E) Schematic of (A) excitatory bipolar cell and (E) inhibitory amacrine cell inputs to A_{ON-S} ganglion cells. (Middle) Example traces of whole-cell voltage-clamp recordings from both control and cone-DTR conditions. (Bottom) Individual isolated (A) mEPSCs and (E) mIPSCs superimposed (black) and average from each recording (green) prior to outlier exclusion from principal component analysis.

(B and F) Amplitudes of isolated (B) mEPSCs and (F) mIPSCs were not significantly different between control and cone-DTR conditions.

(C and G) Frequency of isolated (C) mEPSCs was significantly lower and (G) mIPSCs was significantly higher in cone-DTR retina compared with in control.

(D and H) Integration time of (D) mEPSCs showed no difference and (H) mIPSCs was significantly greater in cone-DTR. Boxplots show median with IQR and whiskers from 10% to 90% of the data.

n indicates number of cells. p values: * ≤ 0.05, ** ≤ 0.01, *** ≤ 0.005.

See also Table S6.

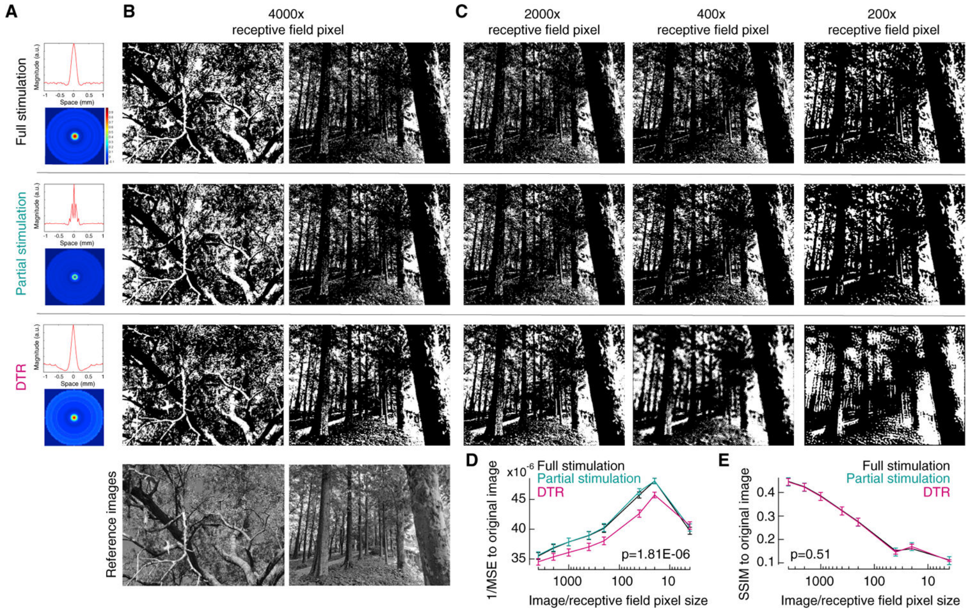

Figure 7. Image filtering by the measured spatial receptive fields reveals that the cone-DTR and control retinas perform similarly with a perceptually based metric

(A) The average linear spatial filters measured from the bar noise stimuli (top) and 3D receptive fields (bottom) of (1) full and (2) partial stimulation of control and (3) cone-DTR retinas.

(B) Example images resulting from convolution of a reference image (bottom) with each of the three spatial filters at image sizes 4,000 times the receptive field pixel size.

(C) Example images resulting from convolution of a reference image with each of the three spatial filters across a range of image sizes.

(D) Inverse of MSE (1/MSE) as a function of image-to-receptive-field pixel ratios.

(E) Structural similarity index (SSIM) of convolved images with the reference image as a function of image-to-receptive-field pixel ratios.

p values: * ≤ 0.05, ** ≤ 0.01, *** ≤ 0.005. See also Table S7.

KEY RESOURCES TABLE

REAGENT or RESOURCE	SOURCE	IDENTIFIER
Antibodies		
Rabbit polyclonal anti-cone arrestin	Millipore	Cat# AB15282; RRID:AB_1163387
Mouse monoclonal anti-gephyrin	Synaptic System	Cat# 147 111: RRID: AB_887719
Rabbit polyclonal anti-VIAAT	Synaptic System	Cat# 132 003: RRID: AB_887869
Mouse monoclonal anti-synaptotagmin II	Zebrafish International resource center	Cat# znp-2: RRID: AB_10013783
Donkey polyclonal anti-mouse-Dylight 405	Jackson Immunoresearch	Cat# 715-475-150; RRID:AB_2340839
Donkey polyclonal anti-mouse-Alexa 647	Jackson Immunoresearch	Cat# 715-605-151; RRID:AB_2340863
Donkey polyclonal anti-rabbit-Alexa 488	Jackson Immunoresearch	Cat# 711-545-152; RRID:AB_2313584
Lectin PNA, Alexa Fluor 647 conjugate	Life technologies	Cat# L32460; N/A
Streptavidin 488	Molecular Probes	Cat# S32354; RRID: AB_2315383
Chemicals, Peptides, and Recombinant Proteins		
Normal Donkey Serum	Jackson Immunoresearch	Cat# NC9624464
Ames' Medium	United States Biological	Cat# A1372-25
Vectashield	Vector Laboratories	Cat# H-1000; RRID: AB_2336789
2-amino-4-phosphonobutyric acid (APB)	Tocris	Cat #0103
Experimental Models: Organisms/Strains		
Mouse model: *Grm6-tdTomato*	(Kerschensteiner et al., 2009)	N/A
Mouse model: *C57BL/6-Gt(ROSA)26Sortm1 (HBEGF)Awai/J (DTR)*	The Jackson Laboratory	Cat# JAX:007900; RRID:IMSR_JAX:007900
Mouse model: *OPNSW1-Cre (BP-Cre)*	(Akimoto et al., 2004)	N/A
Mouse model: OPNMW1-Cre *(HRGP-Cre)*	(Le et al., 2004)	N/A
Software and Algorithms		
ImageJ	NIH	https://imagej.nih.gov/ij/, RRID: SCR_003070
Amira	Thermo-Fisher Scientific	https://www.fei.com/software/amira-avizo/, RRID: SCR_014305
Imaris	Bitplane	https://imaris.oxinst.com/, RRID: SCR_007370
Matlab	Mathworks	https://www.mathworks.com/products/matlab.html, RRID: SCR_001622
Igor Pro	Igor Pro	https://www.wavemetrics.com/, RRID:SCR_000325
Object Finder	(Della Santina et al., 2013	https://github.com/lucadellasantina/ObjectFinder http://doi.org/10.5281/zenodo.4767847
VolumeCut	(Della Santina et al., 2021)	https://github.com/lucadellasantina/VolumeCut http://doi.org/10.5281/zenodo.5048331
Symphony and Stage	Mark Cafaro and Fred Rieke	https://github.com/Symphony-DAS/symphony-v1/wiki https://github.com/Stage-VSS/stage-v1
Image analysis	UPenn Natural Image Database	https://web.sas.upenn.edu/upennidb/albums/